

Do they repeat? Monitoring 36 non-repeating FRBs with FAST

Yuri Uno¹★, Tetsuya Hashimoto¹†, Tomotsugu Goto², Shinnosuke Hisano³, Yi Hang Valerie Wong^{2,4}, Arthur Chen⁵, Sujin Eie^{6,7}, Simon C.-C. Ho^{8,9,10,11}, James O. Chibueze^{12,13,14}, Yu-Wei Lin⁵, Seong Jin Kim², Tzu-Yin Hsu^{5,6}, Poya Wang^{5,6}, Pei Wang^{15,16}, and Murthadza Aznam¹⁷

¹Department of Physics, National Chung Hsing University, No. 145, Xingda Rd., South Dist., Taichung, 40227, Taiwan

²Institute of Astronomy, National Tsing Hua University, No. 101, Section 2, Kuang-Fu Road, Hsinchu City 30013, Taiwan

³Kumamoto University, International Research Organization for Advanced Science and Technology, Kumamoto, 860-8555, Japan

⁴Department of Astrophysical and Planetary Sciences, University of Colorado Boulder, CO 80309, USA

⁵Department of Physics, National Tsing Hua University, 101, Section 2, Kuang-Fu Road, Hsinchu, 30013, Taiwan (R.O.C.)

⁶Institute of Astronomy and Astrophysics, Academia Sinica, 11F of AS/NTU Astronomy-Mathematics Building, No.1, Section 4, Roosevelt Road, Taipei 106216, Taiwan, R.O.C.

⁷Mizusawa VLBI Observatory, National Astronomical Observatory of Japan, 1-2-2 Mizusawa-Hoshigaoka, Oshu, Iwate 023-0861, Japan

⁸Research School of Astronomy and Astrophysics, The Australian National University, Canberra, ACT 2611, Australia

⁹Centre for Astrophysics and Supercomputing, Swinburne University of Technology, P.O. Box 218, Hawthorn, VIC 3122, Australia

¹⁰OzGrav: The Australian Research Council Centre of Excellence for Gravitational Wave Discovery, Hawthorn, VIC 3122, Australia

¹¹ASTRO3D: ARC Centre of Excellence for All-sky Astrophysics in 3D, ACT 2611, Australia

¹²Department of Mathematical Sciences, University of South Africa, Cnr Christian de Wet Rd and Pioneer Avenue, Florida Park, 1709, Roodepoort, South Africa

¹³Centre for Space Research, North-West University, Potchefstroom Campus, Private Bag X6001, Potchefstroom, South Africa, 2520

¹⁴Department of Physics and Astronomy, Faculty of Physical Sciences, University of Nigeria, Carver Building, 1 University Road, Nsukka 410001, Nigeria

¹⁵National Astronomical Observatories, Chinese Academy of Sciences, A20 Datun Road, Chaoyang District, Beijing 100101, People's Republic of China

¹⁶Institute for Frontiers in Astronomy and Astrophysics, Beijing Normal University, Beijing 102206, People's Republic of China

¹⁷Department of Physics, Faculty of Science, Universiti Malaya, Kuala Lumpur, 50603, Malaysia

Accepted 2025 May 28. Received 2025 April 22; in original form 2023 September 30

ABSTRACT

The origin of fast radio bursts (FRBs), highly energetic, millisecond-duration radio pulses originating from beyond our galaxy, remains unknown. Observationally, FRBs are classified as non-repeating or repeating, however, this classification is complicated by limited observing time and sensitivity constraints, which may result in some repeating FRBs being misidentified as non-repeating. To address this issue, we adopt both empirical and machine-learning techniques from previous studies to identify candidates that may have been misclassified. We conducted a follow-up observations of 36 such candidates, each observed for 10 minutes using the Five-hundred-meter Aperture Spherical Telescope (FAST). No radio bursts exceeding a signal-to-noise ratio of 7 were detected, with a typical 7σ fluence limit of ~ 0.013 Jy ms. We constrain the repetition rates of these sources using two statistical models of FRB occurrence. Combining our FAST non-detections with prior observations, we derive upper limits on the repetition rates of $\sim 10^{-2.6} - 10^{-0.22}$ hr⁻¹ under a Poisson process, and $\sim 10^{-2.3} - 10^{-0.25}$ hr⁻¹ under a Weibull process. This work presents one of the most stringent upper limits on FRB repetition rates to date, based on a sample size five times larger than those used in previous studies.

Key words: (transients:) fast radio bursts – radio continuum: transients

1 INTRODUCTION

Fast Radio Bursts (FRBs) are millisecond-scale, highly energetic (up to 10^{42} erg) radio pulses, originating predominantly from extragalactic sources (e.g., Lorimer et al. 2007; Cordes & Chatterjee 2019), with a few rare Galactic exceptions (e.g., Bochenek et al. 2020). Since their discovery in 2007, the origin of FRBs has remained a profound mystery in modern astrophysics, drawing widespread attention from the astronomical community (Lorimer et al. 2007). Interest in this phenomenon has surged, with an increasing number of observational

campaigns devoted to understanding its nature. As of this writing, the number of FRB samples has grown to approximately 800 (Xu et al. 2023).

FRBs are commonly classified as either non-repeaters or repeaters, depending on whether multiple bursts are observed from the same source. Non-repeaters are identified by the detection of a single burst, with no additional bursts observed despite follow-up efforts, while repeaters have produced multiple bursts. Currently, around 60 repeating sources have been confirmed¹.

The separation between repeaters and non-repeaters is not as

★ E-mail: yuri.uno@mail.nchu.edu.tw

† E-mail: tetsuya@phys.nchu.edu.tw

¹ <https://www.chime-frb.ca/repeaters>

straightforward as it appears. Many non-repeaters could, in fact, be repeaters whose subsequent bursts were missed due to limited observing time or the sensitivity thresholds of current telescopes (Caleb et al. 2019; Palaniswamy et al. 2018; Lu et al. 2020; Luo et al. 2018, 2020). Ideally, extensive follow-up observations are necessary to establish an FRB’s repeatability status, but such efforts are resource-intensive. To address this challenge, Hashimoto et al. (2020a) and Chen et al. (2022) proposed alternative classification frameworks based on the statistical analysis of the observed FRB properties.

Hashimoto et al. (2020a) analyzed the time-integrated luminosity-duration relation L_ν - w_{int} and luminosity functions of FRBs, identifying a clear separation between repeaters and non-repeaters. Namely, repeaters tend to exhibit fainter luminosities and longer durations than non-repeaters (see also, Fig. 1).

Chen et al. (2022), meanwhile, introduced a classification scheme using the unsupervised machine learning algorithm Uniform Manifold Approximation and Projection (UMAP). They demonstrated that UMAP can successfully identify repeating FRBs without prior knowledge of their repeatability, and can highlight candidates potentially misclassified as non-repeaters.

This study aims to evaluate the classification schemes proposed by Hashimoto et al. (2020a) and Chen et al. (2022) using the Five-hundred-meter Aperture Spherical Telescope (FAST, Nan et al. 2011), one of the most sensitive single-dish radio telescopes in the world. FAST’s sensitivity surpasses that of other major radio telescopes, including the Canadian Hydrogen Intensity Mapping Experiment (CHIME), Murriyang, the Parkes radio telescope (Parkes), the Upgrade of the Molonglo Observatory Synthesis Telescope (UTMOST), and the Green Bank Telescope (GBT), by more than an order of magnitude. This enhanced sensitivity significantly improves the likelihood of detecting repeating events, which are typically an order of magnitude fainter than single bursts (e.g., Hashimoto et al. 2020a).

In this paper, we report upper limits on FRB repetition rates, derived from the non-detection of repeat bursts in follow-up observations conducted with FAST.

Section 2 describes the criteria and methods used for target selection. Section 3 outlines the optimization of exposure time under the constraint of a 12-hour observation window. Section 4 details the FAST observing campaign and data analysis procedures. Results are presented in Section 5, where we report the non-detection of repeat bursts and establish statistical upper limits on their repetition rates. Finally, Section 6 discusses the implications of our findings, and Section 7 summarizes our conclusions.

2 TARGET SELECTION

We selected our targets from FRBCAT (Petroff et al. 2016) and the first CHIME FRB catalogue (CHIME/FRB Collaboration et al. 2021).

2.1 Empirical method

We employed the physical parameters derived by Hashimoto et al. (2020b), including rest-frame intrinsic durations w_{int} and energy densities L_ν , to identify targets from FRBCAT as of 24 Feb. 2020. The intrinsic duration w_{int} is calculated by correcting the observed duration for instrumental and redshift-related broadening effects (Hashimoto et al. 2019, 2020a,b). Redshifts were estimated from the observed dispersion measures (DMs), unless spectroscopic redshifts were avail-

able (see Hashimoto et al. 2022, for details). L_ν was computed from observed fluence values, integrated over the estimated distance to each FRB. We select non-repeating FRBs from FRBCAT based on the following criteria:

- (A1) $\log L_\nu < 32$
- (A2) $\log w_{\text{int}} > 0.22(\log L_\nu - 32.5) + 0.33$
- (A3) $-14 < \text{Dec} < 66$,

where L_ν , w_{int} , and Declination are in units of erg Hz^{-1} , ms, and deg, respectively.

Criteria (A1) and (A2) were empirically designed to select non-repeating FRBs that lie close to the repeater population in the L_ν - w_{int} parameter space. Criterion (A3) was determined based on the visibility constraints of FAST.

Using these criteria, we identified nine FRBs from FRBCAT as potential targets. Of these, eight were observed with FAST in this study (see Section 4 for details). These eight targets are marked with magenta circles in Fig. 1, and are hereafter referred to as ‘FRBCAT_empirical’ sample. FRBs detected by the Pushchino radio telescope were excluded due to their systematically lower signal-to-noise (S/N) ratios compared to those from other telescopes (Fedorova & Rodin 2019).

For CHIME FRB samples, we employ two distinct methodologies to identify target objects. The first methodology aligns closely with the one delineated above for the FRBCAT sample. In accordance with Hashimoto et al. (2022) and Kim et al. (2022), we applied an empirical selection, w_{int} as a function of energy (E), to the CHIME FRB samples. We select the samples using the following criteria:

- (B1) $\log w_{\text{int}} > -0.25$
- (B2) $\log w_{\text{int}} > 1.7(\log E - 66.5) + 0.25$
- (B3) $-14 < \text{Dec} < 66$
- (B4) $z < 0.3$
- (B5) $|b| > 30$,

where, E is measured in erg units, z is redshift and b represents Galactic latitude, measured in degrees. We incorporate criterion (B4) into the CHIME FRB samples because the disparate distributions of repeating and non-repeating FRBs in the E - w_{int} space are reported for CHIME FRBs at $z < 0.3$ (Kim et al. 2022). We incorporate criterion (B5) to mitigate interference from the elevated radio background originating from the Galactic plane. Applying these criteria yields six CHIME FRBs. In this study, we conducted FAST observations for five of the six identified FRBs (refer to Section 4 for additional details). The five observed FRBs are denoted by magenta circles in Fig. 2. Subsequently, these samples will be referred to as ‘CHIME_empirical’.

2.2 Machine learning method

Another approach applied to the CHIME FRB samples is unsupervised machine learning. Chen et al. (2022) implemented UMAP on the CHIME FRB samples to distinguish between repeater and non-repeater clusters within the high-dimensional FRB dataset. Their findings indicate that 188 non-repeating FRBs are located at clustering regions of confirmed repeaters on the projected UMAP plane (Chen et al. 2022). Although currently unobserved to repeat, these non-repeaters could potentially be authentic repeaters. In this study, we chose 69 repeating FRB candidates as our target samples by applying criteria (B3) and (B5) to the identified 188 potential repeaters. We conducted observations for 25 out of the 69 targets in this work. These samples are henceforth designated as ‘CHIME_ML’. Note

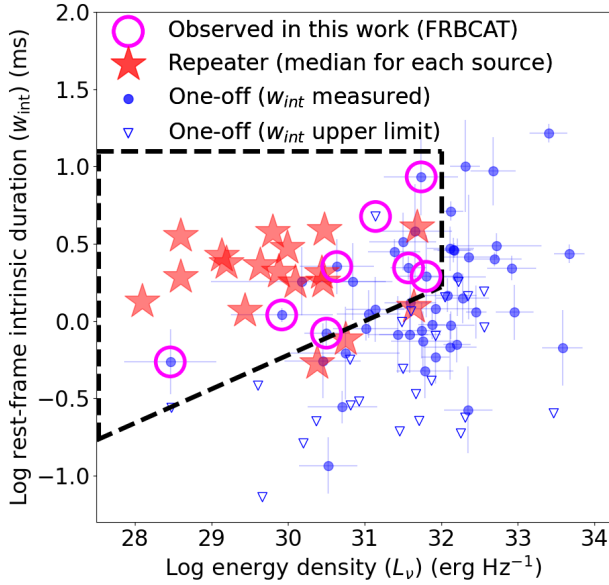


Figure 1. The rest-frame intrinsic duration (w_{int}) of FRBCAT samples (Petroff et al. 2016; Hashimoto et al. 2020b) as a function of the energy density (L_ν). Repeating and non-repeating FRBs are shown by red and blue markers, respectively. Because each repeating FRB source has multiple detections of FRBs, we use the median value to present each repeating FRB source in this diagram. The blue circles and open triangles indicate the measured and upper limit on w_{int} , respectively. The region enclosed by dashed black lines indicates our empirical selection criteria A1 and A2. The magenta open circles mark observed sources with FAST in this work.

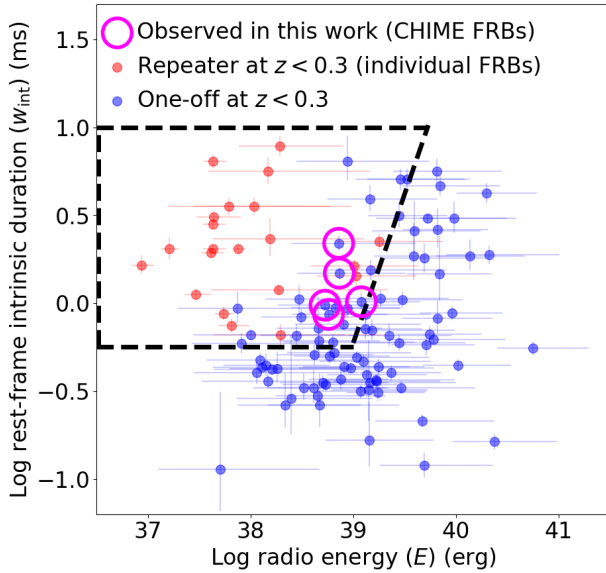


Figure 2. The rest-frame intrinsic duration (w_{int}) of CHIME FRB samples (CHIME/FRB Collaboration et al. 2021; Hashimoto et al. 2022) as a function of the radio energy (E). Repeating and non-repeating FRBs at $z < 0.3$ are shown by red and blue markers, respectively. The individual redshifts of FRB sources are derived from observed DMs unless a spectroscopic redshift is available (see Hashimoto et al. 2022, for details). Individual repeating FRBs are presented in this diagram. The region enclosed by dashed black lines indicates our empirical selection criteria B1 and B2. The magenta open circles mark observed sources with FAST in this work.

that two CHIME sources overlap between CHIME_empirical and CHIME_ML.

3 OPTIMISED EXPOSURE TIME ON EACH SOURCE

Prior to executing our FAST observations, we conduct preliminary Monte Carlo simulations to optimise the exposure time allocated to each source. We operate under the assumption that the chosen samples represent actively repeating FRB sources, each characterized by a specific burst rate, period, and active duration. FRB 20121102A and FRB 20201124A are utilised as case studies within the Monte Carlo simulations. FRB 20121102A is a well-known active repeating FRB source, with a period of approximately 156.1 days and an active phase lasting about 99 days (Wang et al. 2020). This active phase corresponds to a duty cycle of 63.6% (Wang et al. 2020), indicating the proportion of time it remains active within a single period.

Previous FAST observations of FRB 20121102A detected 1652 bursts over a 59.5-hour exposure, corresponding to a burst rate of 28 FRBs hr^{-1} during its active phase (Li et al. 2021). Using these observed parameters, we simulate observations with specific time windows, randomising the observation time within a single period. The total observation time includes the exposure time and a ten-minute overhead for each source.

If the simulated observation falls within the active window of a repeating FRB source, the expected number of FRB detections is calculated as the product of the assumed FRB rate and the exposure time within the active window. Shorter exposure times per source allow for observing a greater number of samples since the total observation time is fixed at twelve hours. In contrast, longer exposure times per source reduce the number of samples observed. A single set of the simulated twelve-hour observations includes exposures on multiple sources and overheads. We repeat the set of observations 10,000 times for a given exposure time on each source. The expected numbers of repeater confirmations are estimated as a function of the exposure time on each source.

Fig. 3 (left) shows the anticipated number of repeater confirmations as a function of the exposure time allocated to each source. These Monte Carlo simulations are based on the observed parameters of FRB 20121102A. The results indicate that shorter exposure times per source increase the likelihood of confirming more repeating FRB sources. This is because even a brief exposure time (e.g., 5–10 minutes) can yield more than one FRB detection if the observation coincides with the source’s active phase, assuming a repeating rate of 28 FRBs hr^{-1} . Identifying a repeater source requires only a single FRB detection. Therefore, allocating shorter exposure times across a greater number of FRB sources increases the likelihood of confirming repeaters, compared to dedicating longer exposures to fewer sources.

FRB 20201124A represents another active repeater observed with FAST (e.g. Xu et al. 2021). Xu et al. (2021) reports over 100 FRB detections from MJD 59305 to 59310, implying an active duration exceeding 6 days. Using the total exposure time of 14 hours at the source², we infer a repeating rate of 7 hr^{-1} during its active phase. As there have been no specific report on the duty cycles of FRB 20201124A to date, we use the duty cycle of FRB 20121102A (i.e., 63.6%; Wang et al. 2020) as reference. This assumption suggests a pattern where FRB 20201124 remains inactive for approximately

² https://fast.bao.ac.cn/observation_log/observed_source_search

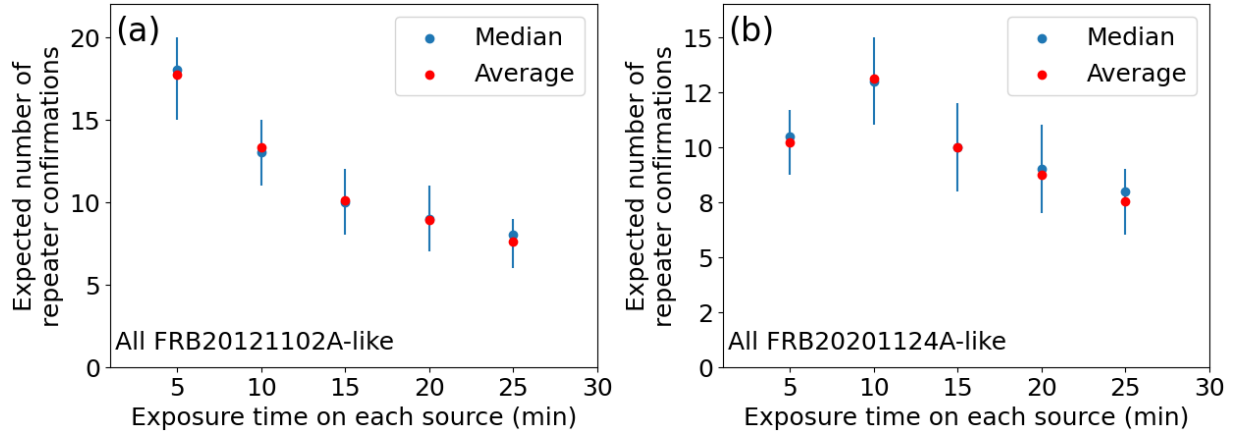


Figure 3. The expected number of repeater confirmations as a function of exposure time on each source derived by Monte Carlo simulations (described in Section 3) in twelve hours of observation time. (Left) The observed parameters of actively repeating FRB 20121102A are assumed. Each blue (red) dot indicates the median (average) value of the number of repeater confirmations over the 10,000 times Monte Carlo simulations for a given exposure time on each source. The blue vertical error bars correspond to $\pm 1\sigma$ data distributions of the Monte Carlo simulations. (Right) Same as left, but assuming FRB 20201124A-like repeating parameters. The duty cycle of FRB 20121102A is assumed.

9.4 days followed by a 6-day active phase. The results of the Monte Carlo simulations, using parameters analogous to FRB 20201124A, are shown in Fig. 3 (right). An exposure time of 10 minutes per source yields the highest number of repeater confirmations.

Monte Carlo simulations based on FRB 20121102A and FRB 20201124A indicate that a 10-minute exposure time per source optimizes the likelihood of confirming repeaters. Therefore, we adopted a 10-minute exposure time for each source in our FAST observations (Section 4). The simulations estimate that approximately ten repeating FRB sources could be confirmed, assuming that all sources observed in this study are active repeaters similar to FRB 20121102A or FRB 20201124A.

4 OBSERVATION AND ANALYSIS

We conducted follow-up observations of 36 repeater candidates, selected based on the criteria outlined in Section 2, using FAST. A summary of the observed sources is provided in Tab. 1 while the telescope specifications are detailed in Tab. 2. The observations were centred at 1.25 GHz in the L band, covering 1.05–1.45 GHz, and employed the pulsar backend in tracking mode. The configurations included full polarisations, a sampling time of 196.608 μ s, and 8192 channels. Each observational block targeted a single source with a 10-minute exposure, scheduled between 4 September 2021 and 22 June 2022, depending on source visibility.

We searched for bursts up to 200 ms in width. The number of channels used for the incoherent dedispersion is 64. Each bin includes 128 frequency channels. Our targets have a median smearing time of ~ 0.12 ms. We calculated the sensitivity losses of our targets using the individual burst duration and DMs, following Karastergiou et al. (2015). The typical sensitivity loss is about 0.1%. The number of polarisations used in our analysis is $n_p = 2$. After the elimination of radio frequency interference by deploying `rfifind` on PRESTO (Ransom 2011), pulse candidates were identified with a S/N threshold of 7. Since the DMs of all targets are known, a lower threshold was regarded as adequate to identify FRBs compared to the typical S/N of 10.

Waterfall plots were generated for each target, focusing on 2.5-second intervals around single-pulse candidates, facilitating thor-

ough visual inspection. In cases where the number of single-pulse candidates for a target exceeded 1,000, we generated a comprehensive waterfall plot covering the full 10-minute exposure time and conducted a detailed visual inspection. However, neither approach revealed any significant signals.

To convey the depth of our visual inspections, we present the two most significant candidates from FRB20181215B and FRB 20181223B in Fig. 4, selected from our data. The dynamic spectra for FRB 20181215B and FRB 20181223B were dedispersed using DM values of 494.0142 pc cm^{-3} and 565.655 pc cm^{-3} , respectively (CHIME/FRB Collaboration et al. 2021), to generate the corresponding waterfall plots (Fig. 4 top). The waterfall plots were integrated over frequency ranges of 1.21–1.39 GHz for FRB 20181215B and 1.13–1.39 GHz for FRB 20181223B to produce the light curves (Fig. 4, bottom).

We fit a single Gaussian function with a constant background parameter (dashed black lines in Fig. 4, bottom) to the peak of each light curve to derive the S/N. The S/N values are estimated to be 3.9 and 4.0 for candidates in the FRB 20181215B and FRB 20181223B data, respectively. Based on these results, we conclude that there is no significant detection in our data with $S/N > 7$.

5 RESULT

Our analysis, employing PRESTO and visual inspections, did not reveal any additional bursts from the 36 repeating FRB candidates. In the following, we estimate the upper limits for the repetition rates of these FRB sources based on our non-detections, building on the analytical framework of Good et al. (2023).

5.1 Sensitivity limit

We determine the sensitivity limit for each source in our observations, following Cordes & McLaughlin (2003), and the equation is as follows:

$$S_{\min} = \frac{\beta S/N(T_{\text{sys}})}{G W_i} \sqrt{\frac{W_b}{n_p \Delta \nu}}. \quad (1)$$

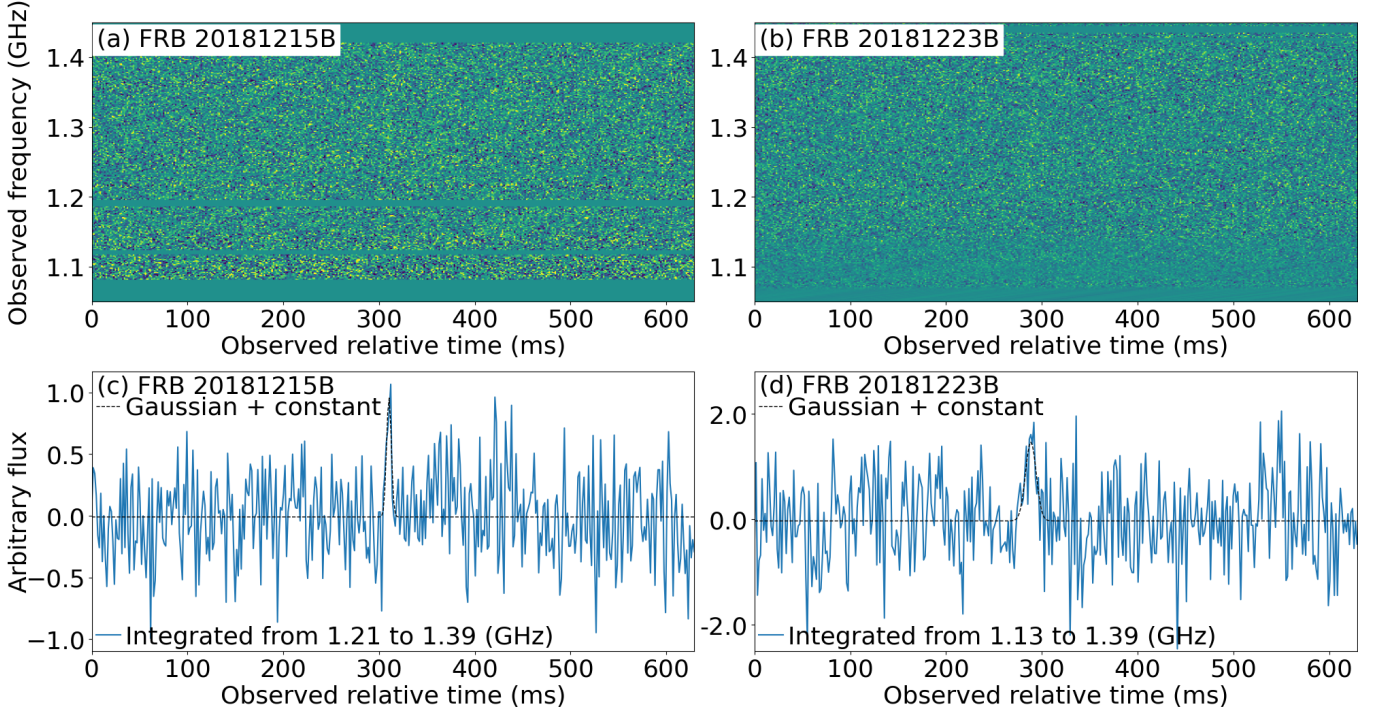


Figure 4. (Top) Waterfall plots of the visually selected pulse candidates from the data of (a) FRB 20181215B and (b) FRB 20181223B. The dynamic spectra were dedispersed using DM values of $494.0142 \text{ pc cm}^{-3}$ for FRB 20181215B and $565.655 \text{ pc cm}^{-3}$ for FRB 20181223B, as reported in [CHIME/FRB Collaboration et al. \(2021\)](#). (Bottom) Light curves (solid blue lines) obtained by integrating the waterfall plots for (c) FRB 20181215B over the frequency range 1.21–1.39 GHz and for (d) FRB 20181223B over 1.13–1.39 GHz. The dashed black line in each panel represent the best fit of a single Gaussian function with a constant background parameter to the measured light curve. The derived S/N values for the candidate signals are 3.9 and 4.0 for FRB 20181215B and FRB 20181223B, respectively.

Here, β represents the digitisation loss. In this work, we adopt the assumption $\beta = 1$ in accordance with [Good et al. \(2023\)](#). T_{sys} is systematic temperature in Kelvin, G is antenna gain in units of K Jy^{-1} , W_i is the intrinsic pulse width in seconds, W_b is the broadened pulse width in seconds, n_p is number of polarisations, and $\Delta\nu$ is frequency bandwidth in hertz. W_b is given as,

$$W_b = \sqrt{W_i^2 + t_{\text{samp}}^2 + t_{\text{chan}}^2 + t_{\text{scatt}}^2}, \quad (2)$$

where t_{samp} is sampling time (s), and t_{scatt} is scattering time (s). t_{chan} is smearing described in [Lorimer & Kramer \(2012\)](#), and as follows:

$$t_{\text{chan}} = 8.3 \mu\text{s} \left(\frac{\Delta\nu_{\text{chan}}}{\text{MHz}} \right) \left(\frac{\nu}{\text{GHz}} \right)^{-3} \left(\frac{\text{DM}}{\text{pc cm}^{-3}} \right), \quad (3)$$

where $\Delta\nu_{\text{chan}}$ is frequency channel bandwidth (MHz) and ν is the central observing frequency (GHz).

The parameters in Eqs. (1) and (2) for each telescope are summarized in Tabs. 1 and 2. These parameters are used to calculate the sensitivities for both original observations and our FAST observations. The scattering time is scaled assuming $t_{\text{scatt}} \propto \nu^{-4}$ to derive values at 1250 MHz, the frequency at which FAST observations are conducted. For some FRBs, no explicit scattering information has been reported. In such cases, we assume the scattering value to be zero.

5.2 Upper limits on the repeating rates

We aim to estimate the upper limits on the FRB repeating rates, assuming both the Poisson and Weibull distributions. The Poisson

distribution models random events occurring at a constant average rate, while the Weibull distribution provides greater flexibility by accommodating clustering events.

5.2.1 Poisson distribution

When N events occur randomly over a time period T with an event rate r , the probability of observing exactly N events in time T follows a Poisson distribution,

$$P(N; rT) = \frac{(rT)^N e^{-rT}}{N!}. \quad (4)$$

The event rate in the Poisson process is given by

$$r = \frac{N}{T}. \quad (5)$$

We modified the Poisson-scaled repeating rate equation from [Good et al. \(2023\)](#), which assumes that FRBs occur randomly within a unit of time and includes a sensitivity scaling factor to make them comparable across different sets of observations. Our modification accounts for the probability of source coverage by FAST. This adaptation allows us to calculate a more accurate upper limit on the repeating rate for each observed source, ($r_{\text{scaled, joint}}$):

$$r_{\text{scaled, joint}} = \frac{N_{\text{bursts}}}{T_P (S_P/S_0)^{-1.5} + P_{\text{acc}} T_F (S_F/S_0)^{-1.5}}, \quad (6)$$

where N_{bursts} is the number of detected bursts, T_P is the on-source exposure time in hours, and S_P is the sensitivity limit in Jansky of previous observations (e.g., CHIME and Parkes). T_F and S_F are the

Table 1. A summary of burst properties of the 36 targets. Rerr represents the error in Right Ascension, measured in degrees, while Derr indicates the error in Declination, also measured in degrees. Note that this Rerr is converted to δ (hour angle) $\times \cos(\text{Decl.})$ so that it can be compared with Derr in degree (Decl.) with the same scale. Rerr for FRB 20181214F is sourced from CHIME/FRB Catalogue Version 1, while errors for other coordinates from CHIME are taken from CHIME/FRB Catalogue Version 2. W_i is intrinsic burst width. The W_i of CHIME sources represents the `width_fitb`, with errors calculated as the sum of `width_fitb_err` for these bursts. The W_i of FRB 20130729 is the reported intrinsic width of < 4 ms. The W_i values for other FRB sources were derived using Eq. (2), based on observed widths reported in the literature, assuming zero scattering where specified. For FRB 20110523A, the unscattered pulse width was 1.73 ms (Masui et al. 2015). The observed widths for FRB 20110703A (< 4.3 ms), FRB 20160410A (4 ms), FRB 20171213A (1.5 ms), FRB 20180212A (1.81 ms) were used to derive their intrinsic widths, assuming no scattering (Thornton et al. 2013; Caleb et al. 2017; Shannon et al. 2018). For FRB 20151230A, the observed width, with scattering effects removed, was reported as 4.4 ± 0.5 ms (Bhandari et al. 2018). Finally, the intrinsic width of FRB 20010621A, also known as J1852–08, was derived from an observed width of 7 ms. $t_{\text{scatt o}}$ is the scattering time reported by original papers. $t_{\text{scatt o}}$ of FRB 20151230A is scaled to 1382 MHz, the center frequency of P(b), from the reported scattering time of 18 ± 6 ms at 1 GHz (Bhandari et al. 2018). Similarly, the $t_{\text{scatt o}}$ of FRB 20130729A is scaled to 1352 MHz from the reported scattering time of 23 ± 2 ms at 1 GHz (Champion et al. 2016; Keane et al. 2011). $t_{\text{scatt FAST}}$ is the scattering time scaled to 1.25 GHz. T_P is exposure time in the original observations in hours. Tel denotes the telescopes that were used for observation, where ‘C’ represents CHIME, ‘G’ stands for GBT, ‘P’ corresponds to Parkes, and letters following ‘P’ represent different observational datasets, with the corresponding references as follows: (a) Thornton et al. (2013), (b) Bhandari et al. (2018), (c) Champion et al. (2016), and (d) Keane et al. (2011). ‘U’ signifies UTMOST, and ‘A’ is for ASKAP. Sel is an abbreviation for the term ‘Selection.’ In the Selection column, ‘E’ denotes empirical selection methods ‘FRBCAT_empirical’ and ‘CHIME_empirical’, while ‘M’ represents machine learning selection methods ‘CHIME_ML’ as defined in Section 2. Properties that were not reported in the original FRB discovery papers are left blank.

FRB ID	RA (J2000)	Rerr (deg)	Dec (J2000)	Derr (deg)	DM (pc cm ⁻³)	W_i (ms)	$t_{\text{scatt o}}$ (ms)	$t_{\text{scatt FAST}}$ (ms)	T_P (hr)	Tel	Sel
20190129A	03:00:24.00	0.196	+21:24:00.0	0.23	484.76 (1)	1.13 (30)	10 (2)	0.5 (1)	13.4 (73)	C	M
20190131B	23:38:48.00	0.235	+11:42:00.0	0.23	1805.729 (4)	0.920 (76)	< 1.1	< 0.06	13.5 (58)	C	M
20190221A	08:50:24.00	0.049	+09:54:00.0	0.26	223.81 (2)	0.97 (13)	0.41 (8)	0.022 (4)	12.0 (68)	C	E
20190226C	01:10:00.00	0.188	+26:45:36.0	0.056	827.77 (2)	1.31 (12)	< 1.5	< 0.08	4.1 (58)	C	M
20190601B	01:11:36.00	0.156	+23:49:12.0	0.036	787.80 (9)	4.04 (36)	5.7 (3)	0.30 (1)	9.6 (73)	C	M
20190604G	08:03:14.40	0.012	+59:30:00.0	0.15	233.05 (1)	1.190 (98)	0.31 (5)	0.017 (3)	27 (12)	C	E
20190605D	01:46:48.00	0.202	+28:36:00.0	0.25	1656.533 (6)	1.069 (87)	< 1.2	< 0.06	11.4 (69)	C	M
20110523A	21:45:12.00	—	−00:09:37.0	—	623.30 (6)	1.304	1.66 (14)	0.28 (2)	0.292	G	E
20110703A	23:30:51.00	—	−02:52:24.0	—	1103.6 (7)	< 4.080	—	—	0.075	P (a)	E
20160410A	08:41:25.00	—	+06:05:05.0	—	278 (3)	3.928	—	—	0.5	U	E
20171213A	03:39:00.00	0.491	−10:56:00.0	0.333	158.6 (2)	0.579	—	—	35.5	A	E
20181203A	02:14:24.00	0.025	+23:36:00.0	0.19	635.926 (2)	0.171 (84)	1.4 (2)	0.08 (1)	14.9 (66)	C	M
20181231A	01:58:48.00	0.159	+21:00:00.0	0.19	1376.732 (2)	0.705 (25)	< 0.76	< 0.04	15.0 (64)	C	M
20190102A	00:37:12.00	0.161	+26:43:12.0	0.057	699.173 (6)	0.824 (73)	0.99 (7)	0.052 (4)	11.5 (81)	C	M
20190118B	02:38:48.00	0.229	+23:36:00.0	0.27	670.9 (2)	3.7 (17)	19 (5)	1.0 (2)	12.4 (78)	C	M
20151230A	09:40:50.00	—	−03:27:05.0	—	960.4 (5)	4.238	4.9 (16)	7.4 (25)	0.15	P (b)	E
20190428A	11:22:55.20	0.025	+23:18:00.0	0.15	969.400 (2)	0.374 (66)	3.6 (4)	0.19 (2)	16.1 (47)	C	M
20181223B	11:39:36.00	0.205	+21:36:00.0	0.24	565.66 (2)	1.57 (31)	4 (1)	0.19 (6)	12.4 (72)	C	M
20190228A	12:13:55.20	0.005	+22:54:00.0	0.12	419.083 (5)	2.25 (10)	18.9 (8)	1.00 (4)	16.0 (50)	C	M
20130729A	13:41:21.00	—	−05:59:43.0	—	861 (2)	< 4	6.9 (6)	9.4 (8)	0.075	P (c)	E
20180212A	14:21:00.00	0.499	−03:35:00.0	0.5	167.5 (5)	1.150	—	—	525.6	A	E
20181128D	14:22:28.80	0.016	+59:54:00.0	0.12	146.501 (4)	1.071 (42)	0.106 (1)	0.00562 (7)	30.9 (67)	C	E
20190111A	14:28:00.00	0.134	+26:48:00.0	0.12	171.9682 (8)	< 1.588 (45)	0.54 (3)	0.028 (1)	16.2 (51)	C	M
20181022E	14:44:48.00	0.187	+27:06:00.0	0.22	285.99 (1)	0.40 (15)	0.63 (9)	0.035 (5)	13.3 (77)	C	M
20190304C	14:52:00.00	0.205	+26:42:00.0	0.25	564.99 (1)	0.948 (89)	< 1.1	< 0.06	12.5 (79)	C	M
20180915B	15:00:48.00	0.227	+25:00:00.0	0.23	177.13 (2)	1.694 (75)	0.111 (8)	0.0059 (4)	13.1 (76)	C	E, M
20181221A	15:22:24.00	0.180	+25:54:00.0	0.21	316.24 (1)	0.754 (83)	1.32 (7)	0.070 (4)	13.4 (76)	C	M
20190125B	15:26:00.00	0.159	+50:30:00.0	0.23	178.24 (2)	2.47 (16)	1.0 (3)	0.05 (1)	17 (11)	C	E, M
20181127A	16:15:12.00	0.208	+25:24:00.0	0.25	930.32 (1)	0.74 (13)	0.58 (9)	0.031 (5)	11.8 (80)	C	M
20190110C	16:28:00.00	0.142	+41:25:12.0	0.050	221.96 (2)	0.390 (76)	0.22 (3)	0.012 (2)	12.4 (97)	C	M
20181228B	16:41:36.00	0.092	+63:54:00.0	0.21	568.651 (2)	< 0.1	1.16 (8)	0.062 (4)	27 (15)	C	M
20181214F	16:50:28.80	0.040	+32:24:00.0	0.22	2105.8 (1)	2.3 (56)	1.5 (3)	0.08 (2)	11.4 (67)	C	M
20190118A	16:53:14.40	0.028	+11:33:00.0	0.084	225.1080 (7)	0.140 (16)	0.282 (6)	0.0150 (3)	11.6 (69)	C	M
20181215B	16:59:12.00	0.115	+47:33:36.0	0.030	494.014 (2)	0.559 (27)	< 0.61	< 0.03	14.1 (9.5)	C	M
20190425A	17:02:48.00	0.130	+21:30:00.0	0.18	128.1577 (2)	0.3799 (20)	< 0.38	< 0.02	16.9 (42)	C	M
20010621A	18:52:05.00	—	−08:29:35.0	—	745 (10)	5.853	< 3	< 4.38	4.2	P (d)	E

on-source exposure time and sensitivity of our FAST observations, respectively. The adopted on-source exposure times and sensitivities are summarised in Tabs. 1 and 3, respectively. S_0 is the reference flux density of 1 Jy (Good et al. 2023). We adopt the power of -1.5 in the flux-density term, which corresponds to the $N_{\text{burst}} \propto S_{\text{min}}^{\alpha}$ ($\alpha = -1.5$) expectation for a non-evolving population in Euclidean space

(e.g. CHIME/FRB Collaboration et al. 2021). The assumed value is consistent with the slope of $\alpha = -1.4 \pm 0.11$ (statistical error) $^{+0.06}_{-0.09}$ (systematic error) measured by CHIME (CHIME/FRB Collaboration et al. 2021). P_{acc} is the probability of the source coverage with FAST,

Table 2. Key properties of FAST, CHIME, Arecibo, GBT, Parkes, UTMOST, and ASKAP observations. The channel width is determined by dividing the bandwidth by the number of channels. The terms T_{sys} , G , n_p , and $\Delta\nu$ in Eq. (1) correspond to the system temperature, antenna gain, number of polarisations, and frequency bandwidth, respectively. In Eq. (2), the term t_{samp} represents the sampling time. In Eq. (3), $\Delta\nu_{\text{chan}}$ and ν denote the channel width and central observed frequency, respectively. The specifications for each telescope were sourced from the following references: CHIME from [CHIME/FRB Collaboration et al. \(2021\)](#), Arecibo from [Good et al. \(2023\)](#); [Deneva et al. \(2013\)](#), GBT from [Masui et al. \(2015\)](#), Parkes (a) from [Thornton et al. \(2013\)](#) Parkes (b) from [Morello et al. \(2020\)](#); [Bhandari et al. \(2018\)](#); [Keith et al. \(2010\)](#) Parkes (c) from [Keith et al. \(2010\)](#); [Champion et al. \(2016\)](#) Parkes (d) from [Manchester et al. \(2001\)](#); [Keane et al. \(2011, 2010\)](#), UTMOST from [Caleb et al. \(2017\)](#), and ASKAP from [Shannon et al. \(2018\)](#); [Bannister et al. \(2017\)](#); [Kumar et al. \(2019\)](#).
* The S/N of the CHIME repeater is 8.5 ([CHIME/FRB Collaboration et al. \(2023\)](#)).

	FAST	CHIME	Arecibo	GBT	Parkes (a)	Parkes (b)	Parkes (c)	Parkes (d)	UTMOST	ASKAP
Centre Frequency (MHz)	1250	600	327	800	1382	1382	1352	1374	843	1320
Frequency Bandwidth (MHz)	400	400	50	200	400	400	340	288	16	336
System Temperature (K)	23	~ 50	115	1.16	21	23	23	21	400	50
Antenna Gain (K/Jy)	16	1.16	10	2	0.735	0.735	0.735	0.735	3	0.1
Sampling Time (μs)	196.608	983	80	1024	64	64	64	250	655.36	126
Number of polarisation	2	2	2	2	2	2	2	2	1	2
Channel Width (MHz)	0.05	0.391	0.025	0.049	0.391	0.391	0.391	1	0.098	1
S/N threshold	7	12*	6	8	9	8	10	8	10	9.5

calculated using the following equation,

$$P_{\text{acc}} = R_{\text{FAST beam}} \times P_{\text{unc}}. \quad (7)$$

where $R_{\text{FAST beam}}$ denotes the ratio of the overlapped area between FAST's 19-beam configuration (defined by its Full Width at Half Maximum, FWHM) and the positional uncertainty area reported in the original detection papers. For a visual representation, see Appendix A, which illustrates the overlap ratio between FAST's 19-beam configuration and the positional uncertainty region. For CHIME-discovered FRBs, the positional uncertainty area is represented as a rectangle. The width of this rectangle corresponds to the right ascension positional error, denoted as R_{err} in Tab. 1, while the height is aligned with the declination positional error, referred to as D_{err} in the Tab. 1. This rectangular representation is chosen because it closely approximates the beam pattern of CHIME, as illustrated in Fig. 6 of [CHIME/FRB Collaboration et al. \(2021\)](#). The positional uncertainty for other FRBs is characterised by elliptical regions. For ASKAP-discovered FRBs, the semi-major and semi-minor axes are represented by R_{err} and D_{err} , respectively. For the rest of FRBs, the semi-major and semi-minor axes are derived from the FWHM values reported by the original FRB discovery papers.

P_{unc} is defined based on the confidence intervals of the uncertainty values reported in the original studies, as the definition of uncertainty varies between works. Specifically, the values assigned to FRBs identified by CHIME, ASKAP, and other sources are 0.68, 0.90, and 0.76, respectively ([CHIME/FRB Collaboration et al. 2021](#); [Shannon et al. 2018](#)). The value of 0.76 is derived based on the assumption that the FWHM of the beam pattern follows a Gaussian distribution.

To estimate confidence intervals for $r_{\text{scaled, joint}}$, we employ the Bayesian approach described by [Kraft et al. \(1991\)](#), which is particularly effective for small observed burst counts, offering more realistic upper limits than Gaussian approximations.

The Poisson upper limits on the repeating rates for the 36 FRB sources, derived using Eq. (6), are shown in Fig. 5.

5.2.2 Weibull distribution

The activity of FRBs may not strictly follow a Poisson process, and the distribution of intervals between bursts can offer more insight than simply analysing the total number of bursts over time. The Weibull distribution provides a generalised probability density function (PDF) for the distribution of intervals between burst events. The

PDF of the time interval between events in a Poisson process is given by

$$p(\delta|r) = re^{-\delta r}, \quad (8)$$

where δ represents the time between consecutive events (i.e., the event interval) and r denotes the constant repetition rate.

The Weibull distribution introduces an additional parameter, k , known as the shape parameter, which characterizes the clustering of FRB activity. In this work, we specifically follow the formalism of [Oppermann et al. \(2018\)](#). The PDF of the Weibull distribution is given by,

$$p(\delta|\tau, k) = \frac{k}{\tau} \left(\frac{\delta}{\tau}\right)^{k-1} e^{-\left(\frac{\delta}{\tau}\right)^k} \quad (9)$$

where τ is the scale parameter, defined as

$$\tau = \frac{1}{r\Gamma\left(1 + \frac{1}{k}\right)} \quad (10)$$

with Γ denoting the gamma function, given by

$$\Gamma(x) = \int_0^\infty dt t^{x-1} e^{-t}. \quad (11)$$

For $k = 1$, the Weibull distribution reduces to the Poissonian case. When $k \neq 1$, the Weibull distribution deviates from Poisson statistics, introducing a clustering effects. In particular, for $k < 1$, the distribution becomes right-skewed, favouring shorter time intervals between events, leading to bursts occurring in clusters.

The posterior PDF of the parameters k and r , conditioned on the observed data, is given by,

$$p(k, r | N, t_1, \dots, t_N) \propto p(N, t_1, \dots, t_N | k, r) p(k, r), \quad (12)$$

where $p(k, r)$ is Jeffreys priors given by,

$$p(k, r) \propto k^{-1} r^{-1}. \quad (13)$$

In our calculations, we adopt the approximation from [Oppermann et al. \(2018\)](#), treating the total likelihood as the product of individual observation likelihoods. This approximation is valid when the time intervals between observations are sufficiently longer than the expected time between successive bursts. Unlike [Oppermann et al. \(2018\)](#), which focused on the analysis of an active repeater, we do not know the typical timescale between successive bursts in our sample.

Table 3. Overview of sensitivity, fluence, positional accuracy, and repeating rate upper limits. S_P is sensitivity limit of prior observations at the time of burst detection, while S_F is the 7σ sensitivity limit of our FAST observations. FL_{\min} is the 7σ fluence limit in Jy ms. P_{acc} is positional accuracy, as detailed in subsection 5.2. r_{scaled} denotes the upper limit on the scaled repeating rate, estimated using two statistical models. $r_{\text{scaled}}(P)$ is based on a Poisson distribution, while $r_{\text{scaled}}(W)$ uses a Weibull distribution. These are indicated by the grey, blue, and red triangles in Figs. 5 and 6. These are indicated by the blue and red triangles in Figs. 5 and 6. The k defines the shape of the Weibull distribution. The r_{scaled} and k values of FRB 20190111A in "This work" is the combined upper limits from CHIME, Arecibo and FAST observations. Similarly, for FRB 20190110C in "This work," they correspond to the combined upper limits from CHIME, CHIME follow-up and FAST observations. For other sources, these values represent the combined rate from prior and FAST observations. The uncertainties are expressed as 90% confidence interval.

FRB ID	CHIME+							This work		
	S_P (Jy)	S_F (Jy)	FL_{\min} (Jy ms)	P_{acc}	$r_{\text{scaled}}(P)$ (hr $^{-1}$)	$r_{\text{scaled}}(W)$ (hr $^{-1}$)	k	$r_{\text{scaled}}(P)$ (hr $^{-1}$)	$r_{\text{scaled}}(W)$ (hr $^{-1}$)	k
20190129A	1.818	0.011	0.014	0.109	$0.18^{+0.54}_{-0.17}$	$0.13^{+0.53}_{-0.12}$	$1.4^{+6.8}_{-1.2}$	$0.048^{+0.14}_{-0.044}$	$0.045^{+0.57}_{-0.042}$	$0.56^{+6.3}_{-0.41}$
20190131B	3.276	0.012	0.013	0.096	$0.44^{+1.29}_{-0.40}$	$0.32^{+1.2}_{-0.30}$	$1.4^{+6.8}_{-1.2}$	$0.071^{+0.21}_{-0.066}$	$0.088^{+1.5}_{-0.083}$	$0.45^{+5.8}_{-0.3}$
20190221A	1.140	0.012	0.011	0.112	$0.10^{+0.30}_{-0.09}$	$0.074^{+0.29}_{-0.069}$	$1.4^{+6.8}_{-1.2}$	$0.040^{+0.12}_{-0.037}$	$0.032^{+0.28}_{-0.030}$	$0.72^{+6.6}_{-0.56}$
20190226C	1.568	0.010	0.013	0.115	$0.48^{+1.4}_{-0.44}$	$0.35^{+1.4}_{-0.33}$	$1.4^{+6.8}_{-1.2}$	$0.047^{+0.14}_{-0.043}$	$0.089^{+1.7}_{-0.085}$	$0.37^{+5.1}_{-0.23}$
20190601B	0.531	0.006	0.023	0.137	$0.040^{+0.12}_{-0.037}$	$0.030^{+0.12}_{-0.027}$	$1.4^{+6.8}_{-1.2}$	$0.013^{+0.037}_{-0.012}$	$0.011^{+0.12}_{-0.01}$	$0.62^{+5.6}_{-0.46}$
20190604G	0.952	0.010	0.013	0.094	$0.034^{+0.10}_{-0.032}$	$0.025^{+0.1}_{-0.023}$	$1.4^{+6.8}_{-1.2}$	$0.023^{+0.066}_{-0.021}$	$0.017^{+0.082}_{-0.016}$	$1.1^{+6.8}_{-0.90}$
20190605D	2.701	0.011	0.013	0.092	$0.39^{+1.1}_{-0.36}$	$0.28^{+1.1}_{-0.27}$	$1.4^{+6.8}_{-1.2}$	$0.065^{+0.19}_{-0.059}$	$0.079^{+1.3}_{-0.074}$	$0.45^{+5.8}_{-0.31}$
20110523A	0.009	0.010	0.014	0.179	$0.0028^{+0.0082}_{-0.0026}$	—	—	$0.0025^{+0.0075}_{-0.0024}$	—	—
20110703A	0.146	0.006	0.023	0.200	$0.74^{+2.2}_{-0.68}$	—	—	$0.012^{+0.036}_{-0.011}$	—	—
20160410A	3.840	0.006	0.022	0.021	15^{+44}_{-14}	—	—	$0.12^{+0.36}_{-0.11}$	—	—
20171213A	12.264	0.015	0.014	0.055	$1.2^{+3.5}_{-1.1}$	—	—	$0.18^{+0.52}_{-0.16}$	—	—
20181203A	10.535	0.036	0.011	0.129	$2.3^{+6.7}_{-2.1}$	$1.6^{+5.1}_{-1.5}$	$1.5^{+6.8}_{-1.3}$	$0.28^{+0.83}_{-0.26}$	$0.40^{+4.8}_{-0.37}$	$0.42^{+5.5}_{-0.27}$
20181231A	3.733	0.014	0.011	0.123	$0.48^{+1.4}_{-0.44}$	$0.35^{+1.4}_{-0.33}$	$1.4^{+6.8}_{-1.2}$	$0.070^{+0.21}_{-0.064}$	$0.094^{+1.6}_{-0.089}$	$0.43^{+5.6}_{-0.29}$
20190102A	2.287	0.013	0.011	0.090	$0.30^{+0.88}_{-0.28}$	$0.22^{+0.86}_{-0.20}$	$1.4^{+6.8}_{-1.2}$	$0.072^{+0.21}_{-0.066}$	$0.07^{+0.94}_{-0.066}$	$0.53^{+6.2}_{-0.38}$
20190118B	0.736	0.006	0.023	0.079	$0.051^{+0.15}_{-0.047}$	$0.037^{+0.15}_{-0.035}$	$1.4^{+6.8}_{-1.2}$	$0.021^{+0.061}_{-0.019}$	$0.016^{+0.14}_{-0.015}$	$0.73^{+6.6}_{-0.57}$
20151230A	0.170	0.008	0.066	0.179	$0.47^{+1.4}_{-0.43}$	—	—	$0.022^{+0.064}_{-0.020}$	—	—
20190428A	6.000	0.021	0.011	0.131	$0.91^{+2.7}_{-0.84}$	$0.66^{+2.5}_{-0.62}$	$1.4^{+6.8}_{-1.2}$	$0.13^{+0.37}_{-0.11}$	$0.17^{+2.7}_{-0.16}$	$0.42^{+5.6}_{-0.28}$
20181223B	1.127	0.009	0.014	0.101	$0.097^{+0.28}_{-0.088}$	$0.071^{+0.28}_{-0.066}$	$1.4^{+6.8}_{-1.2}$	$0.034^{+0.098}_{-0.031}$	$0.028^{+0.28}_{-0.026}$	$0.66^{+6.5}_{-0.5}$
20190228A	1.152	0.008	0.019	0.129	$0.077^{+0.23}_{-0.071}$	$0.057^{+0.22}_{-0.053}$	$1.4^{+6.8}_{-1.2}$	$0.023^{+0.067}_{-0.021}$	$0.02^{+0.24}_{-0.019}$	$0.60^{+6.4}_{-0.44}$
20130729A	0.270	0.009	0.092	0.179	$1.9^{+5.5}_{-1.7}$	—	—	$0.028^{+0.083}_{-0.026}$	—	—
20180212A	6.777	0.011	0.012	0.036	$0.034^{+0.098}_{-0.031}$	—	—	$0.028^{+0.083}_{-0.026}$	—	—
20181128D	0.877	0.011	0.012	0.100	$0.027^{+0.078}_{-0.024}$	$0.02^{+0.077}_{-0.018}$	$1.4^{+6.8}_{-1.2}$	$0.019^{+0.056}_{-0.018}$	$0.014^{+0.063}_{-0.013}$	$1.2^{+6.9}_{-0.98}$
20190111A	0.654	0.009	0.014	0.145	$0.033^{+0.096}_{-0.030}$	$0.024^{+0.095}_{-0.022}$	$1.4^{+6.8}_{-1.2}$	$0.017^{+0.050}_{-0.016}$	$0.0050^{+0.021}_{-0.0050}$	$1.2^{+6.9}_{-0.10}$
20181022E	3.056	0.019	0.009	0.114	$0.40^{+1.2}_{-0.37}$	$0.29^{+1.1}_{-0.27}$	$1.4^{+6.8}_{-1.2}$	$0.10^{+0.30}_{-0.093}$	$0.096^{+1.2}_{-0.090}$	$0.55^{+6.2}_{-0.40}$
20190304C	1.795	0.012	0.011	0.092	$0.19^{+0.56}_{-0.18}$	$0.14^{+0.55}_{-0.13}$	$1.4^{+6.8}_{-1.2}$	$0.058^{+0.17}_{-0.053}$	$0.051^{+0.57}_{-0.047}$	$0.6^{+6.4}_{-0.45}$
20180915B	0.621	0.009	0.015	0.092	$0.037^{+0.11}_{-0.034}$	$0.027^{+0.11}_{-0.025}$	$1.4^{+6.8}_{-1.2}$	$0.022^{+0.064}_{-0.020}$	$0.016^{+0.092}_{-0.015}$	$0.97^{+6.8}_{-0.79}$
20181221A	1.729	0.013	0.010	0.114	$0.17^{+0.50}_{-0.16}$	$0.12^{+0.49}_{-0.12}$	$1.4^{+6.8}_{-1.2}$	$0.054^{+0.16}_{-0.050}$	$0.047^{+0.50}_{-0.043}$	$0.63^{+6.5}_{-0.47}$
20190125B	0.462	0.007	0.018	0.092	$0.018^{+0.054}_{-0.017}$	$0.014^{+0.054}_{-0.013}$	$1.4^{+6.8}_{-1.2}$	$0.013^{+0.037}_{-0.012}$	$0.0092^{+0.044}_{-0.0086}$	$1.1^{+6.9}_{-0.92}$
20181127A	2.927	0.014	0.011	0.092	$0.42^{+1.2}_{-0.39}$	$0.31^{+1.2}_{-0.29}$	$1.4^{+6.8}_{-1.2}$	$0.082^{+0.24}_{-0.075}$	$0.09^{+1.4}_{-0.085}$	$0.48^{+6.0}_{-0.33}$
20190110C	2.775	0.019	0.008	0.112	$0.37^{+1.1}_{-0.34}$	$0.27^{+1.1}_{-0.25}$	$1.4^{+6.8}_{-1.2}$	$0.10^{+0.30}_{-0.09}$	$0.099^{+0.19}_{-0.069}$	$0.93^{+6.4}_{-0.66}$
20181228B	17.028	0.057	0.015	0.106	$2.6^{+7.6}_{-2.4}$	$1.8^{+5.4}_{-1.7}$	$1.5^{+6.8}_{-1.3}$	$0.60^{+1.8}_{-0.55}$	$0.55^{+4.8}_{-0.52}$	$0.56^{+6.2}_{-0.39}$
20181214F	1.417	0.008	0.018	0.127	$0.15^{+0.43}_{-0.14}$	$0.11^{+0.43}_{-0.10}$	$1.4^{+6.8}_{-1.2}$	$0.025^{+0.074}_{-0.023}$	$0.031^{+0.52}_{-0.029}$	$0.45^{+5.8}_{-0.31}$
20190118A	7.764	0.040	0.010	0.123	$1.9^{+5.5}_{-1.7}$	$1.3^{+4.5}_{-1.2}$	$1.5^{+6.8}_{-1.2}$	$0.32^{+0.94}_{-0.29}$	$0.36^{+4.2}_{-0.34}$	$0.47^{+5.9}_{-0.32}$
20181215B	2.838	0.016	0.009	0.165	$0.34^{+0.99}_{-0.31}$	$0.25^{+0.97}_{-0.23}$	$1.4^{+6.8}_{-1.2}$	$0.059^{+0.17}_{-0.054}$	$0.07^{+1.1}_{-0.066}$	$0.46^{+5.8}_{-0.31}$
20190425A	2.271	0.019	0.008	0.138	$0.20^{+0.59}_{-0.19}$	$0.15^{+0.58}_{-0.14}$	$1.4^{+6.8}_{-1.2}$	$0.074^{+0.22}_{-0.068}$	$0.061^{+0.57}_{-0.056}$	$0.68^{+6.6}_{-0.52}$
20010621A	0.136	0.005	0.038	0.201	$0.012^{+0.035}_{-0.011}$	—	—	$0.0058^{+0.017}_{-0.0053}$	—	—

As a result, we cannot strictly verify whether the observation intervals (e.g., ~ 1 day in the CHIME case) are sufficiently long. Nonetheless, this approximation provides a practical solution for analysing discrete, non-continuous observation campaigns where data are not collected over a single uninterrupted time span.

Under this approximation, it is sufficient to consider only two specific scenarios in our study: the probability of observing either zero or one burst within a fixed continuous observation window.

The observations were split into individual blocks, and each block had a continuous exposure time on a source. For instance, CHIME repeats a single-block daily observation, where most blocks include non-detection, and one FRB is detected in one block. We then calculate the combined probability by multiplying the individual probabilities. The probability of observing no events during a single finite observational period is given by,

$$P(N = 0 | k, r) = \frac{\Gamma_i\left(\frac{1}{k}, (\Delta r \Gamma(1 + 1/k))^k\right)}{k \Gamma(1 + 1/k)}, \quad (14)$$

where Δ is the duration of the observational period, expressed in hours throughout this analysis. Γ_i is the incomplete gamma function, defined as,

$$\Gamma_i(x, z) = \int_z^\infty dt t^{x-1} e^{-t}. \quad (15)$$

For CHIME FRB sources, the values of Δ were calculated for each FRB by dividing the reported total exposure time by 80% of the 308-day period from 2018 August 28 to 2019 July 1. Good et al. (2023) noted that approximately 80% of the observation dates (246 days) were considered suitable for scientific observation, taking into account potential interruptions such as system maintenance and weather. Moreover, since the observation time per day was relatively consistent, we assume that dividing the total exposure time by 80% of the total observation days provides a reasonable approximation of the actual observation conditions.

Following Good et al. (2023), Δ is further scaled by sensitivity in the same manner as in the calculation of the Poisson repetition rate (Eq. 4), with an additional scaling factor of P_{acc} , i.e.

$$\Delta_{\text{scaled}} = \Delta(S/S_0)^{-1.5} P_{\text{acc}}, \quad (16)$$

where S is the sensitivity limit. The factor P_{acc} is applied for FAST observations; otherwise, P_{acc} is set to unity. For example, in the case of FRB 20190111A as observed with FAST, Δ_{scaled} is calculated as follows,

$$\Delta_{\text{scaled}} = 10 \text{ min} \times \left(\frac{\text{hour}}{60 \text{ min}}\right) \times \left(\frac{0.009}{1}\right)^{-1.5} \times 0.145 = 28.3. \quad (17)$$

FRB 20190111A is distinctive in that it has been observed by three telescopes: CHIME, Arecibo, and FAST, necessitating a specialized treatment in our analysis.

Good et al. (2023) reported a CHIME exposure time that exceeds the duration recorded in the catalog, spanning from 2018 August 28 to 2021 May 1 (a total of 978 days). Consequently, we adopt their reported exposure time as the CHIME exposure time for this target. To account for the actual observation dates—approximately 80% of the total operational days—we consider 782 days of effective observation. Based on this, Good et al. (2023) reported a total CHIME exposure time of 57.5 hours, yielding a Δ of 57.5/782 hours per day.

For Arecibo observations of the same target, the total exposure time was 3.07 hours over the period from 2019 September 28 to 2019 December 15 (Good et al. 2023). While Good et al. (2023) does not explicitly state the exact number of observation days, private communication with Dr. Good indicates that the observations were

likely conducted over approximately five days within this period. Accordingly, we estimate Δ for Arecibo as 3.07/5 hours per day.

FRB 20190110C is a repeater confirmed at the time of preparing this manuscript (CHIME/FRB Collaboration et al. 2023). The follow-up observations had a total exposure time of 45 ± 11 hours over a period spanning 2019 September 30 to 2021 May 1 (580 days). Similar to FRB 20190111A, we assume that 80% of the 580 days were actual observation days, resulting in $\Delta = 45/464$ hours per day. During these follow-up observations, 2 additional bursts were detected.

The PDF of observing exactly one burst is given by,

$$p(N = 1, t_1 | k, r) = r \text{CDF}(t_1 | k, r) \text{CDF}(\Delta - t_1 | k, r), \quad (18)$$

where t_1 is the time of the first observed burst after the start of a single observation period (Δ). Since the exact time of a burst within an observation session cannot be precisely determined, we set t_1 to be half of Δ . Consequently, the burst is assumed to occur at the midpoint of the observation.

The cumulative distribution function (CDF) is defined as

$$\text{CDF}(\delta | k, r) = \exp\left(-[\delta r \Gamma(1 + 1/k)]^k\right). \quad (19)$$

The upper limits on the repetition rates for the 28 FRB sources detected by CHIME, assuming a Weibull distribution and derived using Eqs. (14) and (18), are shown in Fig. 6.

To obtain the PDF of $\log r$, we marginalized the joint PDF over $\log k$. The integration ranges used are $10^{-2} < k < 10^1$ and $10^{-5} < r < 10^1$. Within this range, the 50th percentile of the resulting r distribution is reported as the upper limit, with the 5th and 95th percentiles representing the associated uncertainties. The values for $\log k$ are obtained similarly, by marginalizing over $\log r$. Examples of the joint PDFs are presented in Appendix B.

This work follows the formalism established in Oppermann et al. (2018) and Good et al. (2023) with a correction for a minor erratum in the calculation code used in Good et al. (2023), as clarified through private communications.

Figs. 5 and 6 represent the calculated upper limits on the repeating rates for the 36 FRB sources, assuming Poisson and Weibull distributions, respectively. The upper limits derived from our FAST observations and prior observations are shown as blue and red triangles, while the results using only prior observations are represented by grey triangles. The CHIME-confirmed repeater is shown by a magenta circle. For the Poisson distribution, the combined upper limits from FAST observations and prior observations range from approximately $10^{-2.6}$ to $10^{-0.22} \text{ hr}^{-1}$. For the Weibull distribution, these limits range from about $10^{-2.3}$ to $10^{0.25} \text{ hr}^{-1}$.

6 DISCUSSION

6.1 Constraints on FRB Repetition Rates and the Weibull Shape Parameter

Good et al. (2023) utilised Arecibo to conduct follow-up observations for seven apparently non-repeating FRB sources to find no additional FRB. Their results place upper limits of $r_{\text{scaled}} \sim 10^{-1.5} \text{ hr}^{-1}$ on the repeating rates of the seven samples. The typical upper limit placed by additional FAST follow-up observations in this work is $r_{\text{scaled}} \sim 10^{-1.3} \text{ hr}^{-1}$ in both Poisson and Weibull cases. This upper limit is comparable to Arecibo's results (Good et al. 2023), while our upper limits include about five times more samples (i.e., non-repeating FRBs) than those reported by Good et al. (2023).

In addition to constraining the repetition rate r , the Weibull distribution also provides implicit constraints on the shape parameter k , which describes the temporal distribution of burst arrival times. We note that the marginalized posteriors typically have broad 90% confidence intervals extending up to $k \sim 6$, indicating that k remains poorly constrained in the absence of detected bursts. Nevertheless, for many sources, the central values (e.g., 50th percentiles) fall below $k = 1$, which may suggest a tendency toward temporally clustered burst behaviour—consistent with previous findings for known repeaters such as FRB 20121102 (Oppermann et al. 2018). However, both clustered and periodic behaviours remain viable under current data. These results underscore the need for extended and continuous observations, along with improved modelling frameworks that incorporate the discrete sampling inherent in follow-up campaigns.

6.2 FRB 20190110C

FRB 20190110C, one of the targets analysed in this study, was originally classified as a non-repeating FRB in the first CHIME FRB catalogue (CHIME/FRB Collaboration et al. 2021). However, in a recent publication, CHIME team reported the discovery of 25 new repeating FRBs (CHIME/FRB Collaboration et al. 2023), six of which were also listed in the first catalogue. Notably, FRB 20190110C, which include three bursts detected with CHIME, is among these newly identified repeaters. This aligns with its classification by the machine-learning method employed in this work, further validating the approach introduced by Chen et al. (2022).

Using the observational parameters reported by CHIME/FRB Collaboration et al. (2023), we calculate the repeating rate of the FRB 20190110C based on Eqs. (6), (14), and (18). The results are depicted as a magenta circle in Figs. 5 and 6 for both Poisson and Weibull repetition models.

In both Poisson and Weibull cases, the derived repeating rates are consistent with the upper limits placed by CHIME and FAST in this work within the errors.

6.3 Positional errors

FAST has 19 beams, each with a size of approximately 0.05 degrees in diameter, resulting in a total field of view of about 0.4 degrees (e.g., Jiang et al. 2020). This field of view is larger than the typical positional error of our targets selected from CHIME FRB, which is around 0.2 degrees (see Tab. 1). The specific beam sizes of other telescopes are as follows. The beam sizes of other telescopes used in FRB discoveries vary significantly. GBT discovered FRB 20110523A with a beam size of ~ 0.3 degrees (Masui et al. 2015). Parkes, through the High Time Resolution Universe (HTRU) survey, identified FRB 20110703A and FRB 20130729A, both with beam sizes of ~ 0.2 degrees (Thornton et al. 2013). Additionally, the SURvey for Pulsars and Extragalactic Radio Bursts (SUPERB) conducted with Parkes detected FRB 20151230A with a beam size of ~ 0.1 degrees (Bhandari et al. 2018). Reanalysis of the Parkes Multibeam Pulsar Survey (PMPS) also identified FRB 20010621A, using a beam size of ~ 0.1 degrees. UTMOST discovered FRB 20160410A with a significantly larger beam size of 4 degrees in the east-west direction, and 2.8 degrees in the north-south direction (Caleb et al. 2017). Meanwhile, ASKAP, using the Commensal Real-time ASKAP Fast Transients (CRAFT), identified FRB 20171213A and FRB 20180212A, both with a beam size of ~ 1 degree (Bannister et al. 2017).

The positional errors and the sensitivity gaps between the 19 beams of FAST mentioned above may account for our non-detection of

subsequent bursts in our repeating FRB candidates. Therefore, we investigated the overlapped area of FAST 19-beams within positional uncertainty (see 5.2 for details). We found out our FAST observations cover about 10% of positional uncertainty as shown in Tab. 3.

7 CONCLUSION

Distinguishing between repeating and non-repeating FRB sources is essential for understanding the mysterious origin of FRBs, as these two classes may arise from fundamentally different progenitors. However, identifying repeating sources requires long-duration, high-sensitivity monitoring, which is observationally expensive and logistically challenging. To address this issue, we selected candidate repeaters among previously non-repeating FRBs using both empirical methods (Hashimoto et al. 2019, 2020a; Kim et al. 2022) and machine-learning techniques (Chen et al. 2022), and conducted follow-up observations with FAST.

We observed a total of 36 non-repeating FRB sources, each with an exposure time of 10 minutes. Notably, one source selected by the machine-learning method was later confirmed by CHIME as a repeating FRB (CHIME/FRB Collaboration et al. 2023). Although the per-source exposure time was relatively short, FAST's exceptional sensitivity increases the likelihood of detecting faint bursts, especially under the assumption of a -1.5 slope in the FRB source count distribution, as reported by CHIME FRBs (CHIME/FRB Collaboration et al. 2021).

The FAST data were carefully inspected down to an S/N ~ 4 after dedispersion using the nominal DM values of each source. No burst candidates exceeding S/N > 7 were identified, corresponding to a typical 7σ fluence limit of approximately 0.013 Jy ms. Our analysis improves the constraints on burst repetition rates by a factor of ~ 3 compared to prior limits, suggesting a typical rate is lower than once per 20 hours, with possible indications of temporal clustering.

This work establishes one of the stringent upper limits on FRB repeating rates to date, based on a sample five times larger than that used in similar previous studies (Good et al. 2023).

ACKNOWLEDGEMENTS

We express our sincere gratitude to Dr. Vishal Gajjar for serving as a referee and for his thorough review and insightful suggestions. His valuable feedback significantly contributed to improving the quality of this manuscript. We would also like to extend our gratitude to Dr. Deborah C. Good for graciously taking the time to answer our questions. YU is also grateful to Dr. Shotaro Yamasaki and Dr. Tomoki Wada for insightful discussions. YU thanks the university for supporting research activities through the NCHU scholarship. TH acknowledges the support of the National Science and Technology Council of Taiwan through grants 110-2112-M-005-013-MY3, 110-2112-M-007-034-, 111-2112-M-005-018-MY3, 112-2123-M-001-004-, 113-2112-M-005-009-MY3, 113-2123-M-001-008-, and Ministry of education of Taiwan through the grant 113RD109. TG acknowledges the support of the National Science and Technology Council of Taiwan through grants 108-2628-M-007-004-MY3, 111-2112-M-007-021 and 112-2123-M-001-004-. SH acknowledges the support of The Australian Research Council Centre of Excellence for Gravitational Wave Discovery (OzGrav) and the Australian Research Council Centre of Excellence for All Sky Astrophysics in 3 Dimensions (ASTRO 3D), through project number CE17010000

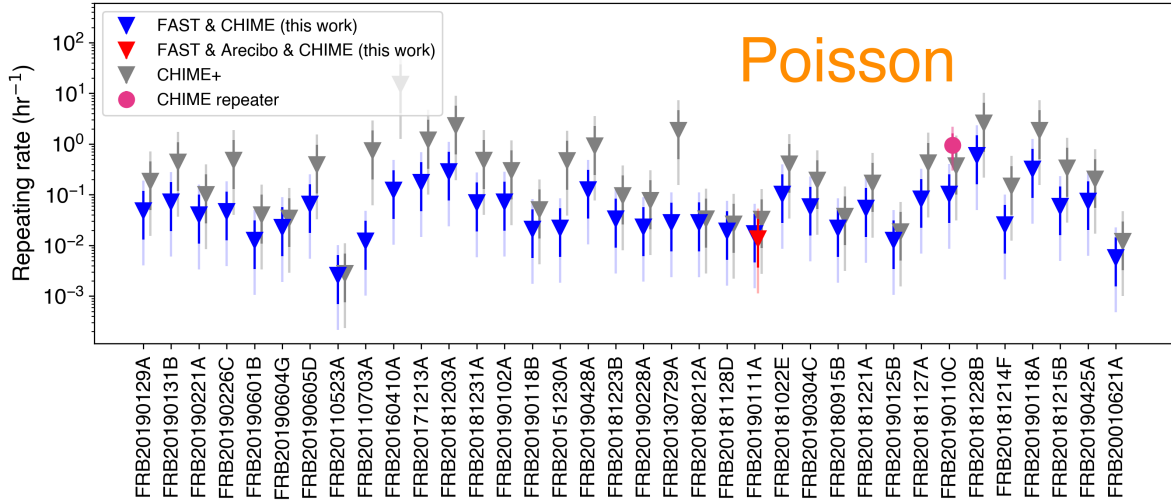


Figure 5. Upper limits on Poissonian repeating rate ($r_{\text{scaled,joint}}$) of 36 FRB sources derived by Eq. (6). Blue triangles indicate joint upper limits obtained by combining prior observations with our follow-up observations, while grey triangles show limits derived solely from prior observations. Coincidentally, Good et al. (2023) conducted a follow-up observation of FRB 20190111A using Arecibo, which overlaps with one of our targets (red triangle). The pink circle represents the repeating rate of FRB 20190110C, which was confirmed as a repeater by CHIME/FRB Collaboration et al. (2023) during the preparation of this manuscript. Its derived repeating rate is 0.95 hr^{-1} . We assume the properties of subsequent bursts are consistent with those of the initial burst, as detailed information was unavailable at the time of writing. Error bars indicate the estimated confidence intervals: solid lines represent the 68% intervals, while lighter, semi-transparent lines correspond to the 90% intervals. Confidence intervals were calculated using the method of Kraft et al. (1991), which provides more accurate estimates when the Poisson event rate is low.

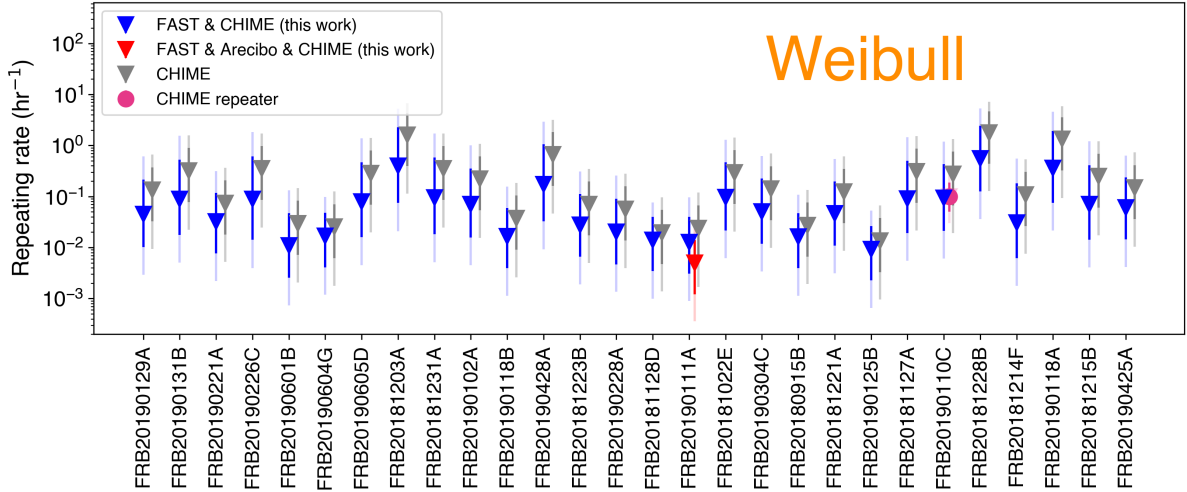


Figure 6. Upper limits on Weibull repeating rate ($r_{\text{scaled,joint}}$) of 28 FRB sources derived by Eqs. (14) and (18). Only CHIME FRB sources are included, with the duration of each daily observation, Δ , provided approximately by Good et al. (2023), a necessary parameter for deriving the upper limit under the Weibull distribution. The setup is otherwise identical to Fig. 5, but with the Weibull model applied. The upper limit on repeating rate on the CHIME repeater FRB 20190110C is $0.142^{+0.106}_{-0.074} \text{ hr}^{-1}$. Error bars on each rate represent the uncertainties derived from the posterior probability distribution of $\log r$. The 50th percentile of the distribution is reported as the upper limit. Solid lines indicate 16th and 84th percentiles, corresponding to the 68% confidence interval, while semi-transparent bars span the 5th to 95th percentiles, representing the 90% confidence interval.

and CE170100013, respectively. JOC acknowledges financial support from the South African Department of Science and Innovation's National Research Foundation under the ISARP RADIOMAP Joint Research Scheme (DSI-NRF Grant Number 150551). We acknowledge the use of the CHIME/FRB Public Database, provided at <https://www.chime-frb.ca/> by the CHIME/FRB Collaboration. This research made use of Astropy, a community-developed core Python package for Astronomy (Astropy Collaboration et al.

2018). This work has used the data from the Five-hundred-meter Aperture Spherical radio Telescope (FAST). FAST is a Chinese national mega-science facility, operated by the National Astronomical Observatories of Chinese Academy of Sciences (NAOC) (Jiang et al. 2019, 2020; Qian et al. 2020).

DATA AVAILABILITY

The data underlying this article has been released from FAST Operation and Development Center and is publicly available under the project ID: PT2021_0076.

REFERENCES

- Astropy Collaboration et al., 2018, *AJ*, **156**, 123
- Bannister K. W., et al., 2017, *ApJ*, **841**, L12
- Bhandari S., et al., 2018, *MNRAS*, **475**, 1427
- Bochenek C. D., Ravi V., Belov K. V., Hallinan G., Kocz J., Kulkarni S. R., McKenna D. L., 2020, *Nature*, **587**, 59
- CHIME/FRB Collaboration et al., 2021, *ApJS*, **257**, 59
- CHIME/FRB Collaboration et al., 2023, *ApJ*, **947**, 83
- Caleb M., et al., 2017, *MNRAS*, **468**, 3746
- Caleb M., Stappers B. W., Rajwade K., Flynn C., 2019, *MNRAS*, **484**, 5500
- Champion D. J., et al., 2016, *MNRAS*, **460**, L30
- Chen B. H., Hashimoto T., Goto T., Kim S. J., Santos D. J. D., On A. Y. L., Lu T.-Y., Hsiao T. Y. Y., 2022, *MNRAS*, **509**, 1227
- Cordes J. M., Chatterjee S., 2019, *ARA&A*, **57**, 417
- Cordes J. M., McLaughlin M. A., 2003, *ApJ*, **596**, 1142
- Deneva J. S., Stovall K., McLaughlin M. A., Bates S. D., Freire P. C. C., Martinez J. G., Jenet F., Bagchi M., 2013, *ApJ*, **775**, 51
- Fedorova V. A., Rodin A. E., 2019, *Astronomy Reports*, **63**, 39
- Good D. C., et al., 2023, *ApJ*, **944**, 70
- Hashimoto T., Goto T., Wang T.-W., Kim S. J., Wu Y.-H., Ho C.-C., 2019, *MNRAS*, **488**, 1908
- Hashimoto T., Goto T., Wang T.-W., Kim S. J., Ho S. C. C., On A. Y. L., Lu T.-Y., Santos D. J. D., 2020a, *MNRAS*, **494**, 2886
- Hashimoto T., et al., 2020b, *MNRAS*, **498**, 3927
- Hashimoto T., et al., 2022, *MNRAS*, **511**, 1961
- Jiang P., et al., 2019, *Science China Physics, Mechanics, and Astronomy*, **62**, 959502
- Jiang P., et al., 2020, *Research in Astronomy and Astrophysics*, **20**, 064
- Karastergiou A., et al., 2015, *MNRAS*, **452**, 1254
- Keane E. F., Ludovici D. A., Eatough R. P., Kramer M., Lyne A. G., McLaughlin M. A., Stappers B. W., 2010, *MNRAS*, **401**, 1057
- Keane E. F., Kramer M., Lyne A. G., Stappers B. W., McLaughlin M. A., 2011, *MNRAS*, **415**, 3065
- Keith M. J., et al., 2010, *MNRAS*, **409**, 619
- Kim S. J., Hashimoto T., Chen B. H., Goto T., Ho S. C. C., Hsiao T. Y.-Y., Wong Y. H. V., Yamasaki S., 2022, *MNRAS*, **514**, 5987
- Kraft R. P., Burrows D. N., Nousek J. A., 1991, *ApJ*, **374**, 344
- Kumar P., et al., 2019, *ApJ*, **887**, L30
- Li D., et al., 2021, *Nature*, **598**, 267
- Lorimer D. R., Kramer M., 2012, *Handbook of Pulsar Astronomy*. Cambridge University Press
- Lorimer D. R., Bailes M., McLaughlin M. A., Narkevic D. J., Crawford F., 2007, *Science*, **318**, 777
- Lu W., Piro A. L., Waxman E., 2020, *MNRAS*, **498**, 1973
- Luo R., Lee K., Lorimer D. R., Zhang B., 2018, *MNRAS*, **481**, 2320
- Luo R., Men Y., Lee K., Wang W., Lorimer D. R., Zhang B., 2020, *MNRAS*, **494**, 665
- Manchester R. N., et al., 2001, *MNRAS*, **328**, 17
- Masui K., et al., 2015, *Nature*, **528**, 523
- Morello V., et al., 2020, *MNRAS*, **493**, 1165
- Nan R., et al., 2011, *International Journal of Modern Physics D*, **20**, 989
- Oppermann N., Yu H.-R., Pen U.-L., 2018, *MNRAS*, **475**, 5109
- Palaniswamy D., Li Y., Zhang B., 2018, *ApJ*, **854**, L12
- Petroff E., et al., 2016, *Publ. Astron. Soc. Australia*, **33**, e045
- Qian L., Yao R., Sun J., Xu J., Pan Z., Jiang P., 2020, *The Innovation*, **1**, 100053
- Ransom S., 2011, PRESTO: Pulsar Exploration and Search ToolKit, Astrophysics Source Code Library, record ascl:1107.017
- Shannon R. M., et al., 2018, *Nature*, **562**, 386
- Thornton D., et al., 2013, *Science*, **341**, 53
- Wang P., et al., 2020, *The Astronomer's Telegram*, **13959**, 1
- Xu H., et al., 2021, *The Astronomer's Telegram*, **14518**, 1
- Xu J., et al., 2023, *Universe*, **9**, 330

APPENDIX A: VISUALISATION OF THE POSITIONAL ERROR REGIONS

For a better understanding of the arguments about the chance of FRB source coverage with FAST (see Section 5.2), we visualise the FAST beams and the positional error of our FRB targets from the original FRB detection papers (CHIME/FRB Collaboration et al. 2021; Shannon et al. 2018). Figs. A1 and A2 show FAST's 19 beams (red) and positional errors of our FRB targets (blue) in the sky. Each figure employs a distinct y-axis scale, which reflects variations in the positional errors of FRBs.

APPENDIX B: POSTERIOR PROBABILITY ON THE WEIBULL MODEL

The two-dimensional posterior PDFs of the event rate r and shape parameter k under the Weibull model, along with their marginalized distributions in terms of $\log r$ and $\log k$, are presented in Figs. B1-B3. Each figure highlights different aspects of the posterior distribution.

Fig. B1 shows the posterir distribution for FRB 20190226C using CHIME data only.

Fig. B2 presents the same source, but with combined CHIME and FAST data. The resulting distribution exhibits a somewhat bimodal structure, due to differences in sensitivity and observing time between the two datasets.

Fig. B3 shows the results for FRB 20190110C—a confirmed repeater—based on combined CHIME, CHIME follow-up, and FAST data. The posterior distributions for $\log r$ and $\log k$ appear more compact, reflecting the increased constraining power the CHIME follow-up observations, during which two additional bursts were detected (CHIME/FRB Collaboration et al. (2023)). This is consistent with the general expectation that combining multiple detection datasets—analogueous to multiplying Gaussian distributions—leads to tighter confidence intervals.

This paper has been typeset from a \LaTeX file prepared by the author.

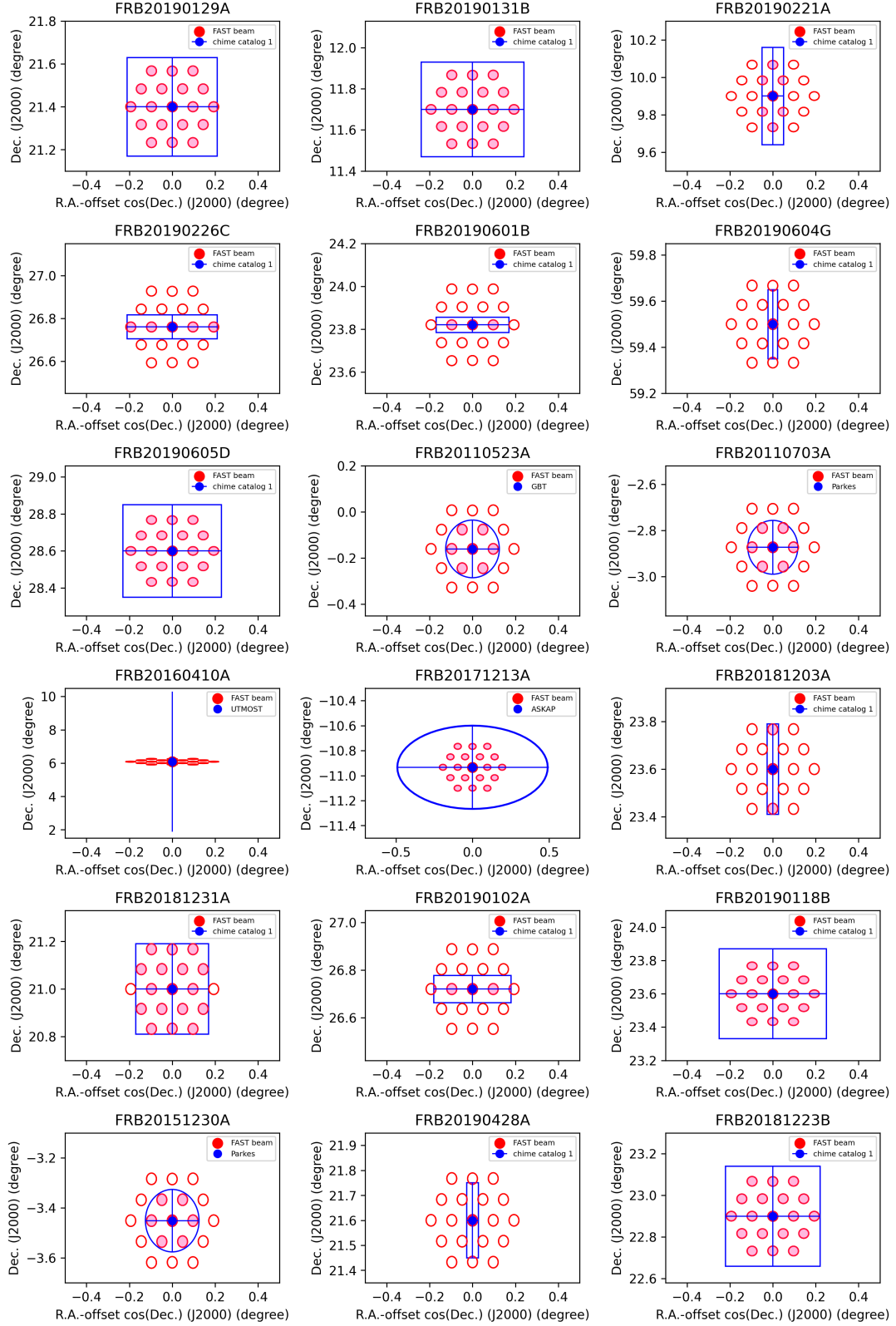


Figure A1. Positional errors of our FRB targets are shown here. The red circles represent the 19 beams of FAST, and the area marked in blue indicates the positional error region reported in the original discovery paper of FRBs (CHIME/FRB Collaboration et al. 2021; Shannon et al. 2018). The region where the FAST beams overlap with the positional error area is coloured in pink. Each figure employs a distinct y-axis scale, which reflects variations in the magnitude of the observed parameters due to different positional errors.

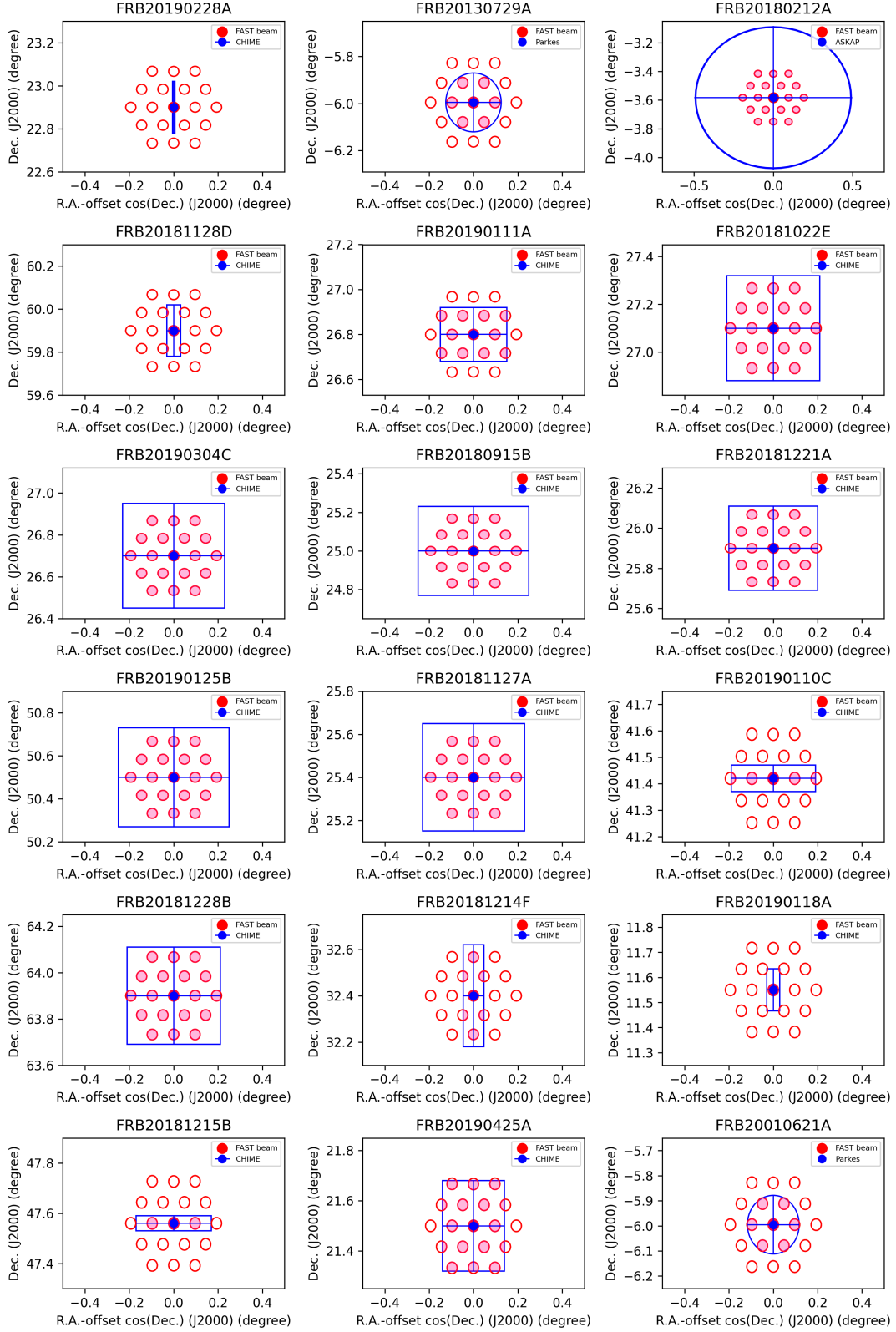


Figure A2. Figure A2 is a continuation of Figure A1.

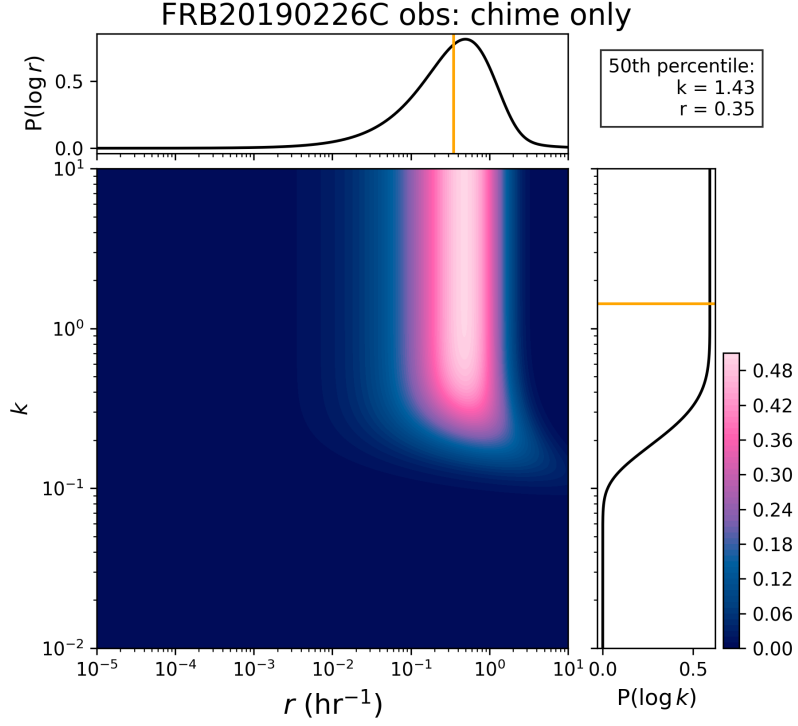


Figure B1. Posterior probability distribution of FRB 20190226C based on CHIME data only. The colour map shows the joint probability density, with pink indicating higher probability regions. The marginalized probability distributions for r and k are shown as black curves along the top and right axes, respectively. The orange line marks the 50th percentile of the marginalized distribution for r and k .

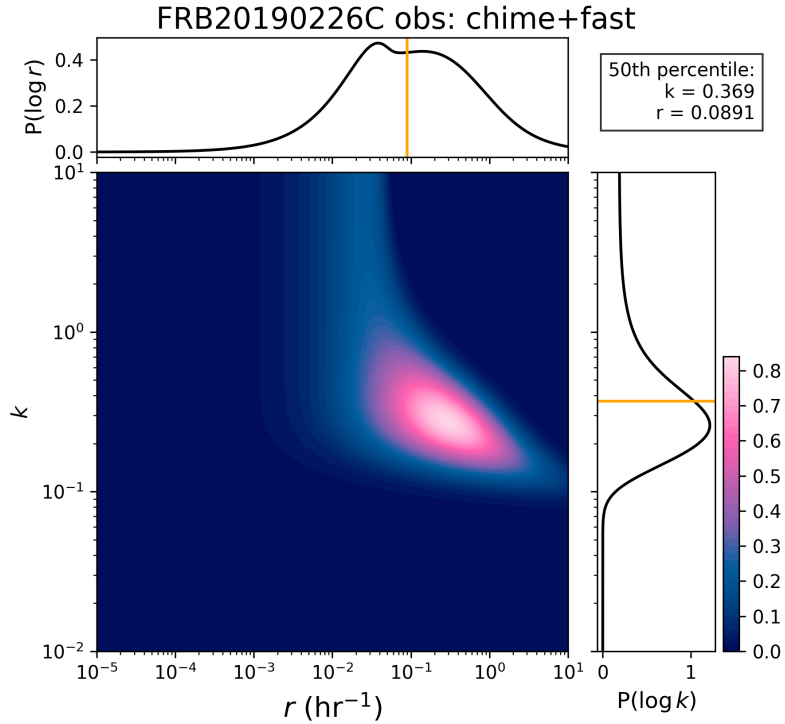


Figure B2. As in Figure B1, but based on the combined CHIME and FAST data for FRB 20190226C.

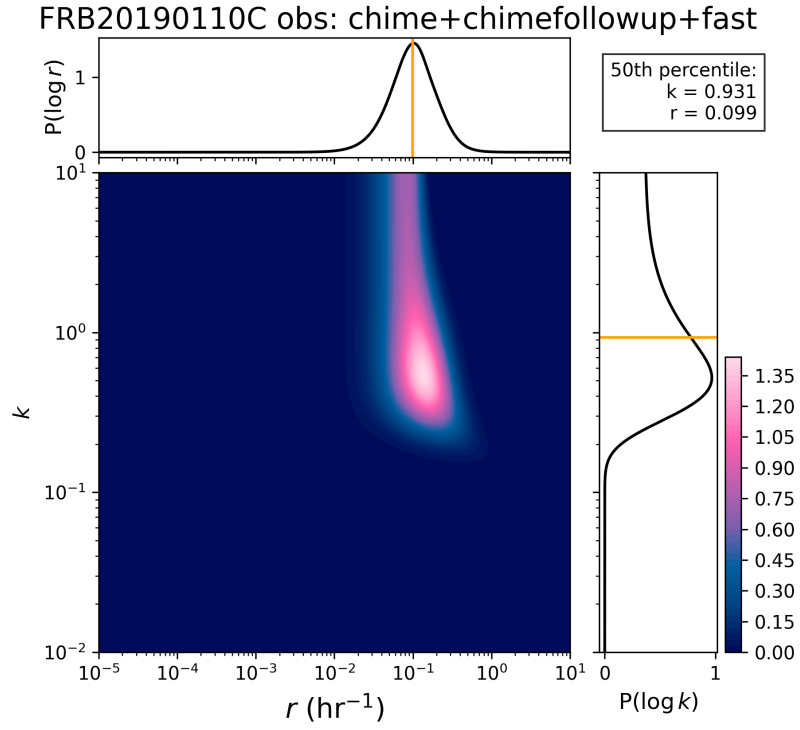


Figure B3. As in Figure B1, but for a different target, FRB 20190110C—confirmed as a repeater by CHIME—with combined CHIME, CHIME follow-up, and FAST data.